Scanning 6-Wavelength 11-Channel Aerosol Lidar

DIETRICH ALTHAUSEN, DETLEF MÜLLER, ALBERT ANSMANN, ULLA WANDINGER, HELGARD HUBE, ERNST CLAUDER,* AND STEFFEN ZÖRNER+

Institute for Tropospheric Research, Leipzig, Germany

(Manuscript received 21 July 1999, in final form 2 December 1999)

ABSTRACT

A transportable multiple-wavelength lidar is presented, which is used for the profiling of optical and physical aerosol properties. Two Nd:YAG and two dye lasers in combination with frequency-doubling crystals emit simultaneously at 355, 400, 532, 710, 800, and 1064 nm. A beam-combination unit aligns all six laser beams onto one optical axis. Hence the same air volume is observed by all six beams. The combined beam can be directed into the atmosphere from −90° to +90° zenith angle by means of a turnable mirror unit. From the simultaneous detection of the elastic-backscatter signals and of the Raman signals backscattered by nitrogen molecules at 387 and 607 nm and by water vapor molecules at 660 nm, vertical profiles of the six backscatter coefficients between 355 and 1064 nm, of the extinction coefficients, and of the extinction-to-backscatter ratio at 355 and 532 nm, as well as of the water vapor mixing ratio, are determined. The optical thickness between the lidar and a given height can be retrieved for all six transmitted wavelengths from measurements under two different zenith angles. In contrast to sun-radiometer observations, this option allows the resolution of spectral extinction information of each of the aerosol layers present in the vertical. The profile of the depolarization ratio is determined at 710 nm and used to investigate particle shape. A few measurement cases are presented to demonstrate the capabilities of the new lidar.

1. Introduction

Tropospheric particles play a major role in many atmospheric processes concerning the earth's radiation budget, air quality, clouds and precipitation, and atmospheric chemistry (Charlson et al. 1992; Penner et al. 1992; Karl et al. 1993; Kiel and Briegleb 1993; Charlson and Heintzenberg 1995; Heintzenberg et al. 1996; Hobbs and Huebert 1996; Quinn et al. 1996). Occurrence, residence time, physical and chemical properties, such as particle size distributions, chemical composition, and corresponding complex refractive index, as well as the resulting optical properties are subject to large diversity especially in the troposphere because of highly different sources and meteorological processes. Therefore, the vertically resolved measurement of physical and spectrally resolved optical properties of particles is of great interest. In addition, the determination of the humidity profile is desirable because of its strong influence on particle properties. In order to meet these requirements, a new tropospheric aerosol lidar has been designed. This contribution describes the new transportable multiple-wavelength lidar system and presents some experimental results.

During the last decades a number of attempts were undertaken to study not only geometrical and scattering properties of aerosol layers, but also to determine basic physical properties of the scatterers with lidars transmitting at several wavelengths. The first systems were comprised of several separate lidars (Reiter et al. 1979; McCormick 1982; Makiyenko and Naats 1983), and allowed the transmission of up to eight wavelengths (Makiyenko and Naats 1983). The simultaneous detection of the same atmospheric volume was not possible with these setups. They therefore only allowed the investigation of the presence and extent of aerosol layers. The prerequirement for the observation of the spatial variability of particle properties was realized by the incorporation of all light sources into one system, which transmitted up to four different wavelengths (Uthe et al. 1982; Kolenda et al. 1992; Stefanutti et al. 1992). Extensive soundings of optical properties of high-altitude clouds and stratospheric particles, mainly generated by the eruption of Mt. Pinatubo, were performed (Makiyenko and Naats 1983; Belan et al. 1992; Burlakov et al. 1992; Stefanutti et al. 1992; Beyerle et al. 1994; McKenzie et al. 1994; Post et al. 1996, 1997; DelGuasta et al. 1994b).

* Current affiliation: Geneva Technology, Frankfurt, Germany.
+ Current affiliation:PC-Ware Information Technologies AG, Leipzig, Germany.

Corresponding author address: Dr. Dietrich Althausen, Institut für Troposphärenforschung, Permoserstr. 15, 04318 Leipzig, Germany.
E-mail: dietrich@tropos.de

With respect to the retrieval of physical particle properties from these backscatter-lidar observations, theoretical studies showed that backscatter coefficients at a minimum of three to four wavelengths are needed to derive physical particle properties (Naats 1980; Zuev and Naats 1983), for example, effective radius, volume, and surface-area concentrations (DelGuasta et al. 1994a; Stein et al. 1994). It was shown that a large amount of a priori information, that is, shape of particle size distribution and complex refractive index, is necessary. In the case of stratospheric soundings in situ measurements (Deshler et al. 1993) provided this information. It was concluded that simple backscatter-lidar systems were restricted to the observation of relatively uniform stratospheric aerosols.

For the above reason only a few attempts have been made to investigate the much more complex characteristics of tropospheric particles. Emphasis was put on the retrieval of optical particle properties (Veretennikov et al. 1979; Uthe et al. 1982; Ivanov et al. 1986; Sasano and Browell 1989; Chaikovsky et al. 1994; McKenzie et al. 1994; Spinhirne et al. 1997). The description of physical properties was restricted to a coarse classification (Ivanov et al. 1986; Sasano and Browell 1989). Not before the 1980s were the demands on multiwavelength tropospheric aerosol sounding with respect to the physical characterization formulated. From theoretical studies it was concluded that for this characterization not only backscatter information, but also extinction information, is necessary (Heintzenberg et al. 1981; Müller 1981; Qing et al. 1989). Results, however, showed that particle size information could only be derived, if the complex refractive index was known as input parameter. At that time, the need for extinction information prohibited any technical realization because lidar measurement methods could not provide this information with the required accuracy (Klett 1981, 1985; Fernald 1984; Sasano et al. 1985; Evans 1987; Ansmann et al. 1992b).

The breakthrough with respect to experimental requirements came in the early 1990s with the development of the high spectral resolution lidar technique (Shipley et al. 1983; Sroga et al. 1983; Grund and Eloranta 1991; Piironen and Eloranta 1994; Eloranta and Piironen 1997) and the Raman-lidar technique (Ansmann et al. 1990; Ansmann et al. 1992a). Both techniques permit one to derive profiles of extinction coefficients with high accuracy. In the late 1990s it could finally be shown that extinction information at two wavelengths is sufficient to derive not only size information but also information on the complex refractive index of the particles, if simultaneous backscatter information at six wavelengths is available (Müller et al. 1999a,b).

The multiwavelength aerosol lidar described in this contribution presents the realization of the experimental and theoretical developments in the field of tropospheric aerosol sounding. Laser pulses at 355, 400, 532, 710, 800, and 1064 nm are emitted simultaneously by means of two Nd:YAG[1] and two dye lasers. The elastically backscattered signals at the six wavelengths, as well as Raman signals of nitrogen at 387 and 607 nm and of water vapor at 660 nm, are detected simultaneously. Polarization discrimination is done by the detection of the cross-polarized signal at 710 nm. From this information profiles of the particle backscatter coefficients at the six wavelengths, the particle extinction coefficient and the lidar ratio at 355 and 532 nm, the depolarization ratio at 710 nm, and the water vapor mixing ratio are derived. Additionally, the system is equipped with a turnable mirror that directs the laser radiation into the atmosphere between $+90°$ and $-90°$ zenith angle. By transmitting laser pulses under different zenith angles the optical thickness at all six wavelengths is determined (Gutkowicz-Krusin 1993; Wallenhauer 1998). The optical properties of the particles serve as input for an inversion scheme that has been specifically designed to determine physical key parameters of atmospheric particles, for example, effective radius, volume, surface area, and number concentrations, as well as mean values of the complex refractive index. This algorithm has been extensively discussed in Müller et al. (1999a,b). A first application to tropospheric particle sounding has been presented in Müller et al. (1998).

After this introduction the experimental setup of the lidar system is given in section 2. In section 3 we briefly summarize the equations from which optical aerosol data are derived. In section 4 we present two measurement examples taken during the Lindenberg Aerosol Characterization Experiment (LACE 98) on 9 and 11 August 1998. The contribution closes with a summary and an outlook.

2. Lidar setup

a. Transmission unit

Figure 1 shows the general setup of the multiple-wavelength lidar inside and outside the container. Two Nd:YAG and two dye lasers are combined into two units A and B on top of each other. Technical specifications of the lasers are summarized in Table 1. The exact wavelengths that are generated are given in Table 2. The Nd:YAG lasers emit at the primary wavelength of 1064 nm with a repetition rate of 30 Hz. The beam diameter is approximately 10 mm, the maximum value of beam divergence is specified to less than 0.5 mrad. Frequency doubling KD*P[2] crystals with conversion efficiencies of approximately 45% are placed behind each of the Nd:YAG lasers and generate light pulses with 532-nm wavelength. In addition, unit A generates laser light at 355 nm through frequency tripling with an additional

[1] Neodymium-doped yttrium aluminum garnet.
[2] KD_2PO_4: Potassium dideuterium phosphate, type II.

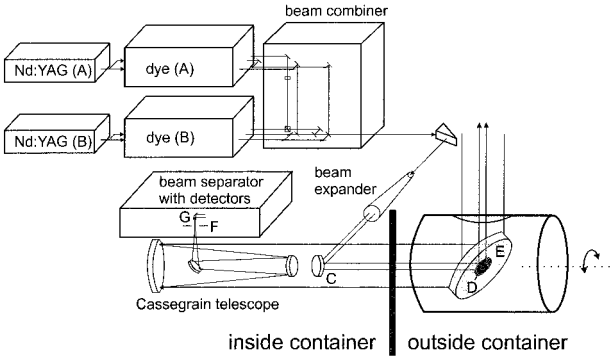

FIG. 1. Schematic diagram of the lidar setup. Two Nd:YAG and two dye lasers in the units A and B transmit radiation at six wavelengths. The beams are aligned onto one optical axis with the beam-combiner unit: C, D, E denote mirrors; F and G are the entrance hole and the off-axis parabolic mirror, respectively. The unit consisting of the mirrors D and E is turnable around the horizontal axis.

KD*P crystal. Its conversion efficiency is 30%. The pulse-to-pulse stability of each Nd:YAG laser is 2% at 1064 nm, 3% at 532 nm, and 4% at 355 nm.

Both Nd:YAG lasers are trigger controlled by delay generators and fired at the same time which results in simultaneous laser pulses at the six different wavelengths. With respect to unit A the light at 1064 nm is dumped, the light at 355 nm and 40% of the one at 532 nm is decoupled with beam splitters before the dye laser. Concerning unit B the light at 1064 and 40% of the one at 532 nm is decoupled with beam splitters before the respective dye laser, as well. All beams are then directed to the beam-combiner unit via folding mirrors. The remaining 60% of the intensity at 532 nm from each Nd:YAG laser is used for optical pumping of the two dye lasers.

The dye laser of unit A generates light pulses at 710 nm, the one of unit B generates light pulses at 800 nm. Unit A uses Pyridin 1 (Brackmann 1994) as laser medium with a conversion efficiency of about 25%, unit B uses Styryl 9M (Brackmann 1994; Exciton 1989) with a conversion efficiency of approximately 5% to 10%. The wavelength of 400 nm is generated through frequency doubling of 800 nm by a BBO[3] crystal with a conversion efficiency of 10% to 20%. The choice of respective wavelengths was determined by technical requirements, for example, the availability of dyes with sufficiently high conversion rates when being pumped (Brackmann 1994), atmospheric-physical constraints such as the absorption of laser radiation by atmospheric trace gases, that is, by ozone, by nitrogen dioxide, and specifically by water vapor (Sidebottom et al. 1972; Molina and Molina 1986; Schneider et al. 1987; Anderson et al. 1993; Burkholder and Talukdar 1994; Ontar Corporation 1994), and requirements concerning data inversion, that is, the retrieval of physical particle parameters from optical extinction and backscatter data (Müller et al. 1999a,b).

The beam-combining unit aligns the laser pulses from units A and B onto one common optical axis by means of dichroic and polarizing elements. Because of this alignment all six beams detect the same atmospheric volume even if the beam is directed into the atmosphere under different zenith angles. Figure 2 shows the general outline of the beam combination. The laser beams exit each of the systems A and B on three separate axes. The pulse at 1064 nm of laser unit B defines the main optical axis. The light at 532 and 1064 nm from units A and B is polarized to 95% to 97%, in the present case perpendicular to the plane of table. This property is made use of in the beam combination by turning the plane of polarization of the light with the wavelength of 532 nm from laser unit A by 90° with the help of a $\lambda/2$ plate. Thus the laser beams of unit A and unit B are cross-polarized to each other and successive polarizing beam splitters combine the laser beams from both units. The combination of light with different wavelengths is done with dichroic beam splitters from long to short wavelengths, as dichroic beam splitters in gen-

[3] β-BAB_2O_4: beta-barium borate.

TABLE 2. Characteristics of emitted laser pulses.

Laser	Wavelength (nm)	Pulse energy (mJ)	Pulse duration (ns)	Beam diameter (mm)
Nd:YAG	1064	500	8–9	9.5
	532	250	6–7	9.5
	355	80	5–6	9.5
Dye	710.724	10	5–8	2.5
	799.857	3	5–8	2.5
	399.928	1.5	4–8	2.5

TABLE 1. Laser characteristics.

Nd:YAG laser	Spectra Physics GCR 5-30
Resonator	Unstable
Pulse repetition rate	30 Hz
Beam divergence (full angle, measured at FWHM points)	$<$0.5 mrad
Dye laser	Lambda Physik LPD 3002
Peak wavelength	697 nm for dye pyridine 1 in polycarbonat 818 nm for dye styryl 11 in methanol
Tuning range	at 710 nm: 673–726 nm (Brackmann 1994) at 800 nm: 780–840 nm (Exciton 1989)
Beam divergence (full angle)	0.5 mrad

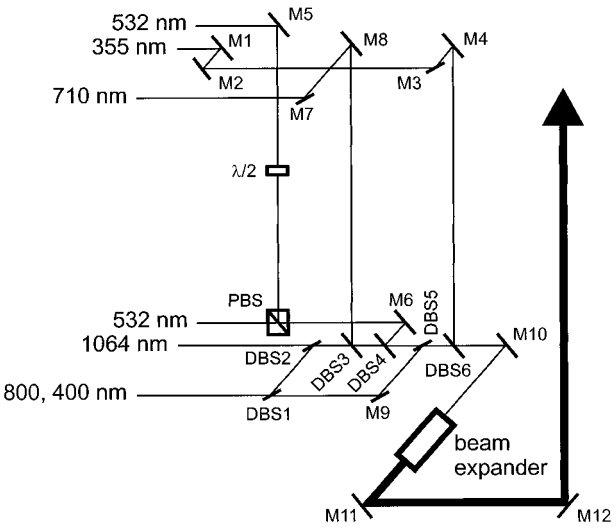

FIG. 2. Beam combiner with mirrors with dichroic coating M1–M9, quartz prism M10, aluminum-coated mirrors M11 and M12, which are the same as mirrors C and D in Fig. 1, polarizing beam-splitter cube PBS, λ/2 plate, and dichroic beam splitters DBS1–DBS6. Optical specifications are given in Table 3. Details of the beam expander are given in Table 4.

eral show better reflection properties for shorter wavelengths and better transmission properties for longer wavelengths. The transmission characteristics of the used dichroic beam splitters are summarized in Table 3. The dichroic beam splitters are not coated on their back surfaces which leads to reflection losses. The diameter of the optical elements is 50 mm.

After the beam combination the divergence of the combined beam is reduced to less than 0.1 mrad by a tenfold beam-expander telescope (see Fig. 1 and Table 4). This in turn increases the diameter of the beams with the wavelengths of 355, 532, and 1064 nm from about 10 to 100 mm and of the beams with the wavelengths of 400, 710, and 800 nm from 2.5 to 25 mm. The laser light is transmitted into the atmosphere via the two plane deflecting mirrors C and D. The diameters are 205 and 150 mm, respectively. Mirror D and the plane deflecting mirror E, with which the backscattered light is collected, are turnable around one common optical axis. These mirrors define the scanning unit. A computer-supported step motor controls the change of angles with a minimum step width of 0.002°. All three mirrors are aluminum-coated for wideband reflection.

TABLE 4. Beam-expander characteristics (Carl Zeiss Jena, Germany).

Objective diameter	100 mm
Objective focal length	998 mm
Expander lens focal length	−100 mm
Calculated Strehl ratio	1064 nm: 78%, 800 nm: 82%, 710 nm: 68%, 532 nm: 91%, 400 nm: 76%, 355 nm: 76%
System magnification	10-fold
Divergence of expanded laser beam	<0.1 mrad

b. Detector unit

The backscattered light is directed by the mirror E onto the main mirror of the focal Cassegrain telescope (see Fig. 1 and Table 5). According to the requirements for sounding particle backscatter and extinction properties in the troposphere, the receiver telescope has to meet two objectives. The diameter of the main mirror should be as large as possible in order to obtain strong signals in the Raman channels and the effective focal length of the telescope should be as short as possible in order to obtain signals as close to the lidar as possible. Hence, a telescope with a parabolic main mirror is necessary. The diameter of the main mirror was set to 530 mm and its focal length to 1666 mm, which yields to an effective focal length of the receiving telescope of 2973 mm (see Table 5).

From the receiver telescope the convergent light beam is directed to the beam-separation unit by a folding mirror that is positioned inside the optical axis of the telescope. The focus of the telescope is located at the aperture F (see Fig. 1). The pinhole determines the field of view of the telescope. It is located right above the bread board onto which the beam-separation unit is mounted. The aperture may be varied between 1 and 17.5 mm in diameter, which results in a field of view between 0.3 and 5.8 mrad. Behind the field stop the beam is deflected and at the same time collimated by an off-axis parabolic mirror G (see Table 5).

Figure 3 shows the beam-separation unit in which the backscattered light is split up with respect to wavelength

TABLE 3. Beam-combiner characteristics: *c*, *p* stand for cross- and parallel-polarized light with respect to the incidence plane.

Dichroic beam splitter	Transmission of front surface (%) at wavelength of nm					
	355	400	532	710	800	1064
DBS1	—	$p > 92$	—	—	$c < 1$	—
DBS2	—	—	—	—	$c < 1$	$p > 96$, $c > 85$
DBS3	—	—	—	$c < 1$	$p > 92$	$p > 95$, $c > 82$
DBS4	—	—	$c < 1$	$p > 98$	$c > 83$	$p > 98$, $c > 83$
DBS5	—	$p < 1$	$c > 83$	$p > 97$	$c > 83$	$p > 98$, $c > 83$
DBS6	p, $c < 1$	$c > 83$	$p > 97$	$c > 82$	$p > 97$	$p > 98$, $c > 80$

TABLE 5. Receiver optics.

Geometry	Focal Cassegrain telescope manufactured by Carl Zeiss Jena, Germany
Diameter of main mirror	530 mm
Aperture	$f/5.6$
Effective focal length	2973 mm
Field of view	0.3–5.8 mrad
Off-axis parabolic mirror	
Diameter	60 mm
Focal length	59.7 mm
Distance between optical and mechanical axis	119.0 mm
Angle between incoming and outgoing beam	90°

and state of polarization and detected in 11 different channels. The main requirements for the system are optimization of the length of the light path through the optics considering the divergence of the light within the separator; choice of beam splitters according to maximum transmission of light for the different channels; and optimization of filters regarding transmission, suppression of background and of elastically backscattered light at the different wavelengths, aging, and temperature dependence.

A lens with a focal length of 1 m is placed in the beam separator between the beam splitters BS1 and BS0 to reduce the diameter of the divergent beam to less than 50 mm at the position of each filter. Because of the reduction of the beam diameter from 530 mm at the main telescope mirror to about 27 mm in the beam separator, the beam divergence is increased by approximately a factor of 20 compared with the receiver field of view.

The beam-separation unit has been optimized for the very weak Raman signals of nitrogen at 387 and 607 nm and of water vapor at 660 nm. In order to keep the losses as small as possible, the Raman signals at the wavelengths of 607 and 660 nm are separated first. Therefore BS1 has a high reflectivity in the band pass between 530 and 680 nm (full width at half maximum). The beam splitter BS6 has to have a sharp edge for the reflection of light with 660-nm wavelength and for the transmission of light with 607-nm wavelength. To increase the performance, the beamsplitter BS6 is used under an incidence angle of 47°. The beamsplitter BS2 is positioned under an incidence angle of 46° for the same reason. The arrangement of the dichroic beam splitters BS0, BS2 to BS5, and BS7 makes use of the fact that beam-splitter efficiency is best when longer wavelengths are transmitted and shorter wavelengths are reflected. The transmission properties of the beam splitters are given in Table 6.

Interference filters are placed in front of each detector. Important optical properties of the filters are given in Tables 7 and 8. The filters are characterized by high transmissions of 38% to 81% at their center wavelengths (Clauder 1996) and very high suppression for the other

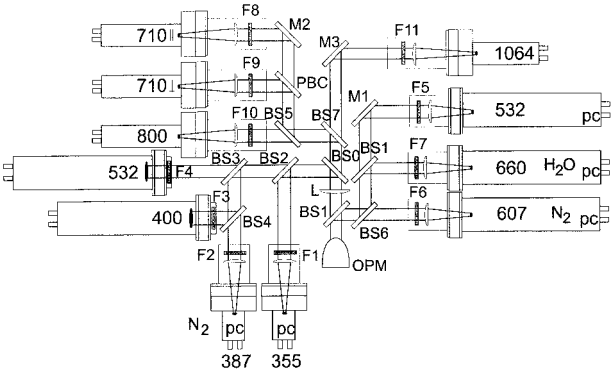

FIG. 3. Beam separator and detectors. An off-axis parabolic mirror OPM (in Fig. 1 denoted with G) is used to deflect the light from the entrance hole toward the different detectors. The backscattered light is spectrally separated by means of beamsplitters BS0–BS7 (see Table 6) and mirrors M1–M3. Here, F1–F11 denote interference filters in front of each detector (see Table 7). Except for the 400-nm and the 532-nm channels a lens is positioned between the filter and the photoactive area of each detector to ensure collection of all backscattered light. An additional lens L between BS1 and BS0 is necessary to reduce the divergence of the incoming beam for complete transmittance through the 50-mm optics. A polarizing beamsplitter cube PBC separates parallel- and perpendicular-polarized light at 710 nm; pc indicates photon-counting channels; and N_2 and H_2O denote the channels for detection of molecular Raman scattering.

TABLE 6. Measured transmission of the beam splitters in percent at the respective wavelengths in nm (1064 nm values from supplier) for cross- (C) and parallel-polarized (P) light. The values for BS2 and BS6 are valid for incidence angles of 46° and 47°, respectively. The incidence angle of 45° is valid for the rest of the beam splitters. For BS4 only values for 355–400 nm are essential due to its position in the beam separator.

		355	387	400	532	607	660	710	800	1064
BS0:	C	3		1	2	9	83	68	89	78
	P	1		<1	1	87	94	85	99	89
BS1:	C	68		60	45	2	3	72	73	80
	P	92		89	69	1	1	99	96	92
BS2:	C	1		78	77	82	73	75	68	80
	P	1		95	96	94	96	96	91	95
BS3:	C	16		5	84	64	69	82	65	80
	P	73		3	95	90	90	95	84	90
BS4:	C	91	91	<1						
	P	92	94	50						
BS5:	C	25		51	30	11	3	4	83	81
	P	74		80	80	83	2	1	99	95
BS6:	C	1		71	77	85	<1	1	49	75
	P	19		91	93	95	2	27	92	90
BS7:	C	25		57	56	35	3	4	6	81
	P	73		88	86	86	21	1	3	98

TABLE 7. Filter characteristics in beam-separation unit. The suppression between 200 and 1200 nm amounts to 10^{-5} (10^{-3}%) relative to the transmission maximum of the filter. Coating provided by Barr Association Inc. and Andover Corporation.

Filter no.	Maximum transmission wavelength (nm)	FWHM (nm)	Transmission at the maximum (%)
1	354.67	0.35	38
2	386.3	2.8	73
3	399.93	0.33	60
4	532.17	1.1	67
5	532.5	5	75
6	607.7	3	73
7	660.9	3	71
8	710.06	0.40	64
9	710.07	0.37	64
10	799.91	0.42	55
11	1064.0	5	81

TABLE 8. Suppression characteristics of the filters 2, 6, and 7 for the Raman channels with respect to the other wavelengths (nm). The transmission between 200 and 1200 nm amounts to 10^{-5} relative to the transmission maximum of the filter. Coating provided by Barr Ass. Inc.

Filter no.	355	400	532	710	800	1064
2	10^{-8}	$<10^{-5}$	10^{-8}	$<10^{-5}$	$<10^{-5}$	10^{-8}
6	10^{-5}	10^{-6}	10^{-8}	10^{-6}	10^{-6}	10^{-5}
7	10^{-9}	10^{-9}	10^{-10}	10^{-10}	10^{-9}	10^{-7}

wavelengths; for example, the filter of the Raman water vapor channel at 660 nm has to suppress light with a wavelength of 532 nm by 10 orders of magnitude in order to avoid cross-sensitivities. The filter bandwidths were chosen to be 3 nm for the Raman channels at 387, 607, and 660 nm. The filter bandwidths of the channels at the elastic-backscatter wavelengths from 355 to 800 nm were set to 0.4 nm. These channels are operated under daytime conditions and the small bandwidth provides the necessary reduction of the background radiation from the atmosphere. The filter bandwidths of the elastic-backscatter channels at 532 and 1064 nm are set to 5 nm, since the emitted power at these wavelengths is larger than 200 and 400 mJ, respectively, so that the atmospheric background has less influence.

After passing the interference filters the signals are detected by photomultipliers. The detectors were optimized with respect to the size of their photosensitive area, their quantum efficiency, and their dark current. Respective values are given in Tables 9 and 10. Because of the small photosensitive areas of the analog channels at 710, 800, and 1064 nm, as well as of the photon-counting channels at 355, 387, 532, 607, and 660 nm, lenses are placed directly behind the interference filters which focus the beams onto the respective detectors.

The signal-processing unit is shown in Fig. 4, a few technical properties are given in Tables 11 and 12. The elastic-backscatter signals, except at 355 nm, are detected in the analog mode. The photon current is changed into a proportional electron current and consecutively converted into a voltage signal by means of transimpedance amplifiers. The 12-bit analog–digital converters digitize the signals with a tact frequency of 10 MHz, which corresponds to a spatial resolution of 15 m. The A/D conversion is controlled by a frequency generator, which also provides the laser repetition rate of 30 Hz with a fixed delay. Fast input buffers store the data. After reaching the block length, which corresponds to the maximum resolvable range of the lidar, the buffers are switched into the transfer mode. The data are read out by three digital signal processors, analyzed with respect to under- or overflow, rejected if necessary, and finally averaged across a set number of laser pulses. The digitizing errors are less than 1/4096. The transimpedance converters are set in the way that the noise is 1.5 times the least significant bit. The averaged signal profiles are stored by a personal computer.

TABLE 9. Detector characteristics of the analog channels.

Wavelength (nm)	Model	Photosensitive surface area (mm)	Dark current (nA)	Quantum efficiency (%)
400	THORN EMI PMT 9214QB	46	5	26
532	THORN EMI PMT 9817QB	46	<100	10
710	Hamamatsu R2228	25	<2	3.5
800	Hamamatsu R2228	25	<6	1.5
1064	Hamamatsu R632	15	<6	>0.03

TABLE 10. Detector characteristics of photon-counting channels.

Wavelength (nm)	Model	Photosensitive surface area (mm)	Dark counts (counts per second)	Quantum efficiency (%)
355	Hamamatsu R5600P-03	8	55	21
387	Hamamatsu R5600P	8	31	19
532	THORN EMI 9893A/350	9	30	10
607	THORN EMI 9893A/350	9	94	4
660	THORN EMI 9893A/350	9	19	7

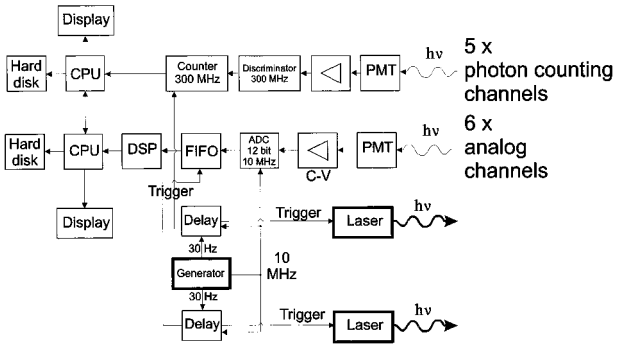

FIG. 4. Data acquisition with five photon-counting and six analog channels for the simultaneous recording of the different signals. PMT stands for photomultiplier tube, C–V denotes current-to-voltage converter, and ADC analog-to-digital converter. FIFO is the first-in-first-out buffer, DSP the digital signal processor, and CPU the central processing unit.

The detection of the very weak Raman signals at 387, 607, and 660 nm, of the elastic-backscatter signal at 355 nm, and of part of the 532-nm backscatter signal is done by photon counting. The voltage pulses at the exit of the respective detector are amplified 10 times. Discriminators reduce the dark signals. Finally the pulses are detected by a 300-MHz counting system on a time-resolved base and stored by a personal computer after accumulation of a certain number of laser pulses. The smallest available time window is 100 ns, which is equivalent to a spatial resolution of 15 m. The entire photon-counting system is operated with a maximum count rate of 10^7 Hz in order to avoid saturation effects and signal-induced noise. If necessary, signals are reduced with neutral-density filters in front of the interference filters.

Simultaneous to signal acquisition the raw data are transferred to a personal computer and displayed online as a color-coded plot. This quick-look feature serves as a fast way of monitoring the measurement in terms of instrument performance, atmospheric conditions, and present particle layers.

c. Stability and alignment

The entire system is mounted in a framework, which contains optical benches to avoid any movement of the components against each other. The framework is kept free from vibration from the floor by buffers. The detection unit had been adjusted only once by means of laser diodes which define the optical axis. The elements are fixed on an optical bench. The detection unit prooved to be excellently aligned even after a two-month transport of the container by truck and by ship. During an experiment only the laser beams have to be aligned onto the optical axis. Because each laser beam is folded by at least two elements of the beam-combining unit, it can easily be directed onto the common optical axis. This alignment is done by directing the beams through a variable field stop in front of the beam expander. The observation of diffraction rings on a screen which is placed behind the beam expander permits to align the beams with a maximum deviation of 0.5 mm m^{-1} distance, which corresponds to an angle of 0.5 mrad. Consequently, the receiver field of view is set to 0.8 mrad to assure that the laser beams cannot leave it.

No severe misalignments of the system could be observed over a period of many days. There are different indicators to check stability and alignment. First of all, stability shows itself in the fact that no realignment of the laser beams is necessary even after many days of operation of the system. Furthermore, the alignment can be checked from respective online presentations of the raw signals of each channel during the measurement. One of the indicators is the height at which the maximum of the signals caused by complete overlap of laser beam and receiver field of view is reached. Any severe changes of this height for individual channels would clearly show a deterioration of the alignment. Another indicator is the observed structure of cirrus clouds. An identical fine structure of all elastic-backscatter signals with height indicates that all beams met the same volume of the cloud. Finally, misalignments would clearly be identified during signal processing, for example, backscatter and extinction profiles would not reach background values above any aerosol and cloud layers.

TABLE 12. Characteristics of photon-counting system.

Preamplifier	Thorn EMI A2H, rise time 2.5 ns
Discriminator	Phillips Scientific, model 704
Data acquisition system:	
Type	5-input-channel multichannel scaler
Model	Medav Purana
Maximum count rate	300 MHz
Minimum time-bin width	100 ns
Number of time bins	1024

3. Data evaluation

In this section a brief overview of the methods is given, with which the optical particle parameters are calculated from the measured elastically and inelasti-

TABLE 11. Characteristics of analog system.

Preamplifier: 400, 532 nm	FEMTO Messtechnik HCA-S, bandwidth 4 MHz
Preamplifier: 710, 800, 1064 nm	Romanski Sensor- und Verstärkertechnik V4 Special, bandwidth 5 MHz
Analog–digital converter	Intelligent Instrumentation ZPD 1002 Burr Brown ADC 603, 12 bit, 10 MHZ
Input buffer	Intelligent Instrumentation ZPB 6064
Digital signal processors	Intelligent Instrumentation ZPB 34A

cally scattered signals. Furthermore, some error estimation is performed. For the inversion of microphysical particle properties, the optical data are needed with an accuracy of better than 10% to 15% (Müller et al. 1999a,b). It should be mentioned that all methods, namely, the Klett method, the Raman-lidar method, and the scanning method, are well known. The errors connected with them have been intensively discussed (Ansmann et al. 1992a,b; Ferrare et al. 1998a,b; Gutkowicz-Krusin 1993). However, the combination of different methods in general leads to an improvement of the results compared to the separate use of the different methods, as discussed below.

The basic lidar equations are

$$P(R, \lambda) = P_0 \frac{F(R, \lambda)}{R^2} [\beta_\lambda^{\text{par}}(R) + \beta_\lambda^{\text{mol}}(R)] \exp\left\{-2 \int_0^R [\alpha_\lambda^{\text{par}}(r) + \alpha_\lambda^{\text{mol}}(r)]\, dr\right\}, \quad (1)$$

$$P(R, \lambda_{\text{ra}}) = P_0 \frac{F(R, \lambda_{\text{ra}})}{R^2} N_{\text{ra}}(R) \frac{d\sigma(\pi, \lambda_{\text{ra}})}{d\Omega} \exp\left\{-\int_0^R [\alpha_\lambda^{\text{par}}(r) + \alpha_\lambda^{\text{mol}}(r) + \alpha_{\lambda_{\text{ra}}}^{\text{par}}(r) + \alpha_{\lambda_{\text{ra}}}^{\text{mol}}(r)]\, dr\right\}. \quad (2)$$

Here, $P(R, \lambda)$ and $P(R, \lambda_{\text{ra}})$ denote the received signal power from distance R at the laser wavelength λ and at the Raman-shifted wavelength λ_{ra}, respectively; P_0 is the power of the emitted laser pulse; and F contains the efficiency of the receiver optics and the detectors as well as the geometrical overlap function. The latter describes the overlap between the laser beam and the receiver field of view of the telescope. Also, $\beta_\lambda^{\text{par}}$ and $\beta_\lambda^{\text{mol}}$ are the volume backscatter coefficients for particle and molecular backscattering, respectively; $\alpha_\lambda^{\text{par}}$, $\alpha_\lambda^{\text{mol}}$, $\alpha_{\lambda_{\text{ra}}}^{\text{par}}$, and $\alpha_{\lambda_{\text{ra}}}^{\text{mol}}$ denote the volume particle and molecular extinction coefficients for the elastic and the Raman-shifted wavelengths, respectively; and N_{ra} is the molecule number density of the Raman-active gas and $d\sigma(\pi, \lambda_{\text{ra}})/d\Omega$ the range-independent differential Raman cross section for backscattering.

With the Raman-lidar technique profiles of extinction and backscatter coefficients can be derived with high accuracy. The data evaluation starts with the derivation of the extinction profiles from the nitrogen Raman profiles (Ansmann et al. 1990):

$$\alpha_\lambda^{\text{par}}(R) = \frac{\dfrac{d}{dR} \ln \dfrac{N_{\text{ra}}(R)}{R^2 P(R, \lambda_{\text{ra}})} - \alpha_\lambda^{\text{mol}}(R) - \alpha_{\lambda_{\text{ra}}}^{\text{mol}}(R)}{1 + \left(\dfrac{\lambda}{\lambda_{\text{ra}}}\right)^{k(R)}}. \quad (3)$$

The only input parameter is the wavelength dependence k of the aerosol extinction coefficient between the primary (355, 532 nm) and the Raman wavelengths (387, 607 nm). A wrong estimation of k, for example, $k = -0.5$ is assumed and $k = -1.0$ is true, leads to negligible errors of $\alpha_\lambda^{\text{par}}$ of the order of 3% (Ansmann et al. 1992b). In addition, the height profiles of Rayleigh extinction $\alpha_\lambda^{\text{mol}}(R)$ and of the nitrogen number density $N_{\text{N2}}(R)$ must be known. These profiles are usually determined from actual radiosonde data of pressure and temperature with negligible errors (Ansmann et al. 1992b). If radiosonde data are not available, they may be obtained with sufficient accuracy from a standard-atmosphere model.

The backscatter coefficients at 355 and 532 nm are calculated from the ratio of the elastic-backscatter and the Raman signals next (Ansmann et al. 1992b):

$$\beta_\lambda^{\text{par}}(R) = -\beta_\lambda^{\text{mol}}(R) + [\beta_\lambda^{\text{par}}(R_0) + \beta_\lambda^{\text{mol}}(R_0)] \times \frac{P(R_0, \lambda_{\text{ra}}) P(R, \lambda) N_{\text{ra}}(R)}{P(R_0, \lambda) P(R, \lambda_{\text{ra}}) N_{\text{ra}}(R_0)} \times \frac{\exp\left\{-\displaystyle\int_{R_0}^R [\alpha_{\lambda_{\text{ra}}}^{\text{par}}(r) + \alpha_{\lambda_{\text{ra}}}^{\text{mol}}(r)]\, dr\right\}}{\exp\left\{-\displaystyle\int_{R_0}^R [\alpha_\lambda^{\text{par}}(r) + \alpha_\lambda^{\text{mol}}(r)]\, dr\right\}}. \quad (4)$$

Here, the only input parameter is the particle backscatter coefficient $\beta_\lambda^{\text{par}}(R_0)$ at a specific distance R_0. This reference value is usually chosen such that $\beta_\lambda^{\text{mol}}(R_0) \gg \beta_\lambda^{\text{par}}(R_0)$. Appropriate regions of clear air can be identified from the extinction profiles derived before. The resulting error is less than 5% to 10% (Ansmann et al. 1992b; Ferrare et al. 1998a,b). Profiles of molecular extinction and backscattering for λ and λ_{ra} are again calculated from radiosonde data. The particle extinction-to-backscatter, or lidar, ratio at 355 and 532 nm is directly obtained once $\alpha_\lambda^{\text{par}}$ and $\beta_\lambda^{\text{par}}$ are known:

$$S_\lambda^{\text{par}}(R) = \frac{\alpha_\lambda^{\text{par}}(R)}{\beta_\lambda^{\text{par}}(R)}. \quad (5)$$

Summarizing the Raman method one can state that systematic errors because of not exactly known input parameters play only a minor role and lead to errors of less than 10%. Because Raman signals are comparably weak, the statistical error due to photon noise is much more important. Sufficient integration in time and space is thus necessary to reduce the overall statistical error

(signal noise and background noise) to less than 10%. Typical integration values are 30 min and 60 m in the planetary boundary layer (lowest 1 to 2 km) and 1 h and 180 m above. The stability of the atmospheric conditions during the period of time for which the profiles are averaged is checked on the base of high-resolution (15 m, 30 s) time–height contour plots. Averaging errors do not play a role in the case of aerosol measurements, because the typical weak changes in aerosol conditions can be expected to have linear influence on the signals (Ansmann et al. 1992b).

The backscatter coefficients at 400, 710, 800, and 1064 nm are determined with the so-called Klett method, that is, by solving a Bernoulli equation that is derived from the basic lidar equation (1) (see, e.g., Klett 1981, 1985; Fernald 1984; Sasano et al. 1985). Before applying the Klett method the signals must be sufficiently averaged so that the overall statistical error is less than 5%. The solution can be written as (Fernald 1984)

$$\beta_\lambda^{\text{par}}(R) = -\beta_\lambda^{\text{mol}}(R) + \frac{A(R_0, R, \lambda)}{B(R_0, \lambda) - 2S_\lambda^{\text{par}} \int_{R_0}^{R} A(R_0, r, \lambda)\, dr}, \quad (6)$$

with

$$A(R_0, x, \lambda) = x^2 P(x, \lambda) \times \exp\left[-2(S_\lambda^{\text{par}} - S^{\text{mol}}) \int_{R_0}^{x} \beta_\lambda^{\text{mol}}(\zeta)\, d\zeta\right]$$

and

$$B(R_0, \lambda) = \frac{R_0^2 P(R_0, \lambda)}{\beta_\lambda^{\text{par}}(R_0) + \beta_\lambda^{\text{mol}}(R_0)}.$$

Here, $S^{\text{mol}} = 8\pi/3$ sr is the molecular extinction-to-backscatter ratio, and $S_\lambda^{\text{par}}(R)$ and the particle backscatter coefficient $\beta_\lambda^{\text{par}}(R_0)$ at a specific distance R_0 must be estimated.

The most critical input parameter in the Klett solution for $\lambda \leq 532$ nm is the range-dependent lidar ratio $S_\lambda^{\text{par}}(R)$. If no additional information is available, it causes errors of the order of 100% (Ansmann et al. 1992b). Because in our case the lidar ratio at 355 and 532 nm is known from the Raman method, a good estimate of this input parameter for the Klett solution, especially for the critical wavelength of 400 nm, is possible. The reference value plays only a minor role for the short wavelengths and is set, as for the Raman solution, such that $\beta_\lambda^{\text{mol}}(R_0) \gg \beta_\lambda^{\text{par}}(R_0)$. Thus the backscatter coefficient at 400 nm can be determined with an error below 10%.

For longer wavelengths, the critical input parameter is the reference value $\beta_\lambda^{\text{par}}(R_0)$. The lidar ratio is not important here, because it is needed to correct for the atmospheric transmission effect, which is small for the longer wavelengths. If one takes the lidar ratio as it is determined at 532 nm with the Raman method as input parameter, errors of less than 5% in the backscatter coefficients at 710, 800, and 1064 nm are obtained (Wallenhauer 1998). The clear-air assumption for the reference value is difficult to apply for wavelengths $\lambda >$ 700 nm because of weak Rayleigh scattering. If the elastic-backscatter signals are integrated with the same time and height resolution as the Raman signals, Rayleigh scattering can serve for calibration up to the wavelength of 800 nm, and the respective error is estimated to be less than 10%. For the wavelength of 1064 nm the reference height R_0 should be located inside a layer with low, but still detectable particle scattering. The Raman solutions at 355 and 532 nm serve to identify appropriate layers. The reference value is found by extrapolating the results achieved for wavelengths between 532 and 800 nm at this height. Care should be taken in the use of backscatter coefficients at 1064 nm in the inversion scheme, because errors may be of the order of 20% to 30%. The calibration of the long wavelengths can be done more accurately, if the reference height R_0 can be set into a cirrus layer as particle backscattering is neutral in this case (Ansmann et al. 1993) and short-wavelength values in the cirrus can directly serve as reference values for the long wavelengths.

In summary, it can be stated that the careful evaluation of the combined information of elastic and inelastic backscattering at different wavelengths leads to trustworthy profiles of particle extinction and backscatter coefficients with errors of less than 10% to 15% as required by the inversion scheme.

An additional method to obtain atmospheric optical properties is the determination of optical-depth profiles by the detection of elastically (or inelastically) backscattered signals at a given wavelength for two different zenith angles θ_1 and θ_2 of the laser beam. Considering the angle dependence of the height $z = R\cos(\theta)$, Eq. (1) becomes

$$P(z, \theta_i) = P_0 \frac{K \cos^2(\theta_i)}{z^2} \beta_{\theta_i}(z) \times \exp\left[-\frac{2}{\cos(\theta_i)} \int_0^z \alpha_{\theta_i}(\zeta)\, d\zeta\right], \quad (7)$$

with $i = 1, 2$. The optical depth $\tau(z)$ between the lidar ($z = 0$) and the height z is then directly given by (Hamilton 1969; Gutkowicz-Krusin 1993; Wallenhauer 1998)

$$\tau(z) = \int_0^z \alpha(\zeta)\, d\zeta = -\frac{\cos\theta_2 \cos\theta_1}{2(\cos\theta_2 - \cos\theta_1)} \ln\frac{P_{\theta_1}(z) \cos^2\theta_2}{P_{\theta_2}(z) \cos^2\theta_1}. \quad (8)$$

The fundamental condition, that has to be fulfilled here, is horizontal and temporal homogeneity. Whether or not the same aerosol structures were monitored under the

TABLE 13. Parameters from multiwavelength lidar at respective wavelengths (nm).

Parameter	From	355	400	532	710	800	1064
β	Klett method [See Eq. (6)]	×	×	×	×	×	×
β	Raman method [See Eq. (4)]	×		×			
α	Raman method [See Eq. (3)]	×		×			
S	Raman method [See Eq. (5)]	×		×			
τ	Scanning method [See Eq. (8)]	×	×	×	×	×	×
Δ	Ratio of cross- to parallel-polarized signals				×		
m	Ratio of water vapor Raman to nitrogen Raman signals						

respective zenith angles can simply be checked by comparing the signal profiles at θ_1 and θ_2 that are used in Eq. (8).

Finally, the water vapor mixing ratio $m(R)$ can be determined from the ratio of the water vapor Raman signal at 660 nm to the nitrogen Raman signal at 607 nm (Melfi et al. 1969; Ansmann 1992a) and the particle depolarization ratio, containing information about the sphericity of the scatterers (Schotland et al. 1971; Sassen 1991), is simply obtained by forming the signal ratio $\Delta = P_\perp/P_\parallel$ of the cross- and parallel-polarized signals measured at 710 nm. Table 13 summarizes the information that is provided by the system.

4. Measurement examples

Two measurement examples are briefly discussed to demonstrate the performance of the aerosol lidar described above. The observations were made during the Lindenberg Aerosol Characterization Experiment 1998 (LACE 98) that was conducted about 60 km southeast of Berlin, Germany, in the summer of 1998. The main goal of this aerosol field campaign was the characterization of anthropogenically influenced European aerosols and the estimation of their climate forcing. The first example shows a measurement in a heavily polluted boundary layer, the second one an observation of a free-tropospheric aerosol layer, which was advected from a forest-fire region in western Canada according to back-trajectory analysis.

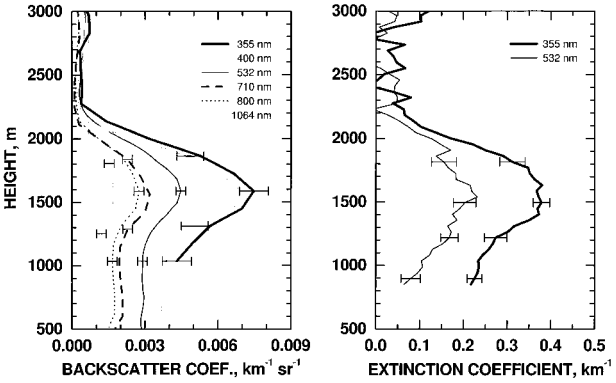

FIG. 5. Mean particle backscatter and extinction coefficients determined with the multiwavelength lidar in the heavily polluted boundary layer on 11 Aug 1998 between 2021 and 2221 UTC. The lidar was operated at a zenith angle of 40°. Backscatter signals measured with 15–60-m resolution were smoothed with window lengths of 180 (backscatter) and 420 m (extinction). Error bars indicate the standard deviation caused by signal noise and uncertainties in the input parameters needed to solve Eqs. (3), (4), and (6).

With respect to the first example, we selected a period of 2 h for further data evaluation based on a careful evaluation of the time series of the individual profiles of the entire observational period. In Fig. 5, the particle backscatter and extinction coefficients are given. The 355-nm signal profile could not be evaluated below 1000 m because of misalignment of the receiver optics. As mentioned in section 3, an accurate calibration of the signal profiles for the wavelengths ≥710 nm in height regions with very low aerosol content is, in most cases, not satisfactory. The presence of an ice cloud between 9- and 10-km heights was used here to calibrate the backscatter-coefficient profiles. It was assumed that ice-crystal backscattering is wavelength independent, so that the backscatter coefficients for all measurement wavelengths are equal. The assumption is valid for typical ice clouds with particle diameters much larger than the laser wavelength. The lidar ratio at 400 nm was obtained from the interpolation between the values at 355 nm (about 50 sr between 1400 and 1700 m) and at 532 nm (about 45 sr between 1400 and 1700 m). For the wavelengths ≥710 nm 40 sr was used.

In Fig. 6, the solution for the 532-nm backscatter coefficient is shown between the ground and 4000 m height together with the water vapor mixing ratio, which was determined from the ratio of the water vapor Raman signal to the nitrogen Raman signal. The profile of the relative humidity was calculated from the mixing ratios and from temperatures measured with radiosonde at the lidar site. The simultaneous detection of aerosol optical properties and relative humidity is necessary in climate-impact studies, because moisture strongly influences the observed particle optical properties.

The profiles in Fig. 6 are standard products of Raman-lidar observations. The main advantage of these observations is that they are not affected by the so-called overlap effect. The incomplete overlap between the laser beam and the receiver field of view is often not well defined below about 1000 m and can have, even in the case of correction, considerable influence on the lidar profiles for heights below 500 m. The Raman-lidar solutions, however, are determined from signal ratios. Provided that the detector channels are well aligned, both

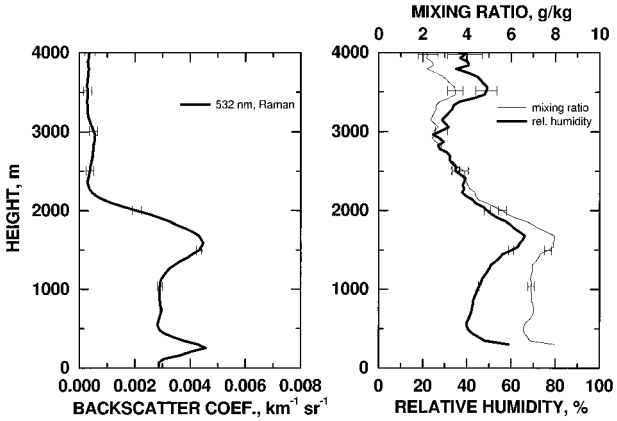

FIG. 6. Mean particle backscatter coefficient and water vapor mixing ratio determined by applying the Raman-lidar method [Eq. (4); Melfi et al. 1969] for the same time period as shown in Fig. 5. The relative humidity is calculated from the mixing ratio and from the temperature measured with radiosonde. In the case of the humidity values, lidar signals are smoothed with window lengths of 180 and 240 m below and above 1500 m, respectively. Error bars show the standard deviation due to statistical and systematic uncertainties.

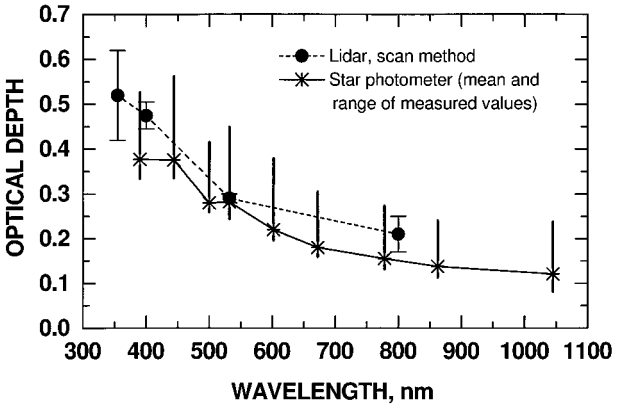

FIG. 7. Spectrally resolved mean particle optical depth derived from scanning-lidar and star-photometer observations on 11 Aug 1998 between 2330 and 0030 UTC. The lidar was run alternately at the two zenith angles of 30° and 60°. At each position lidar return signals were averaged over 5 min. Error bars indicate the standard deviation due to signal noise. The photometer values are calculated after the so-called two-star method (Leiterer et al. 1995, U. Leiterer 1998, personal communication). The range of photometer values obtained between 2330 and 0030 UTC is marked by vertical lines.

signal profiles are affected in the same way by the overlap effect. By forming signal ratios, geometrical effects should cancel out completely. In Fig. 6, this is true for the backscatter coefficient. Unfortunately, the water vapor Raman channel was not well aligned and thus the water-vapor profiles were useful only for heights above 250 m, as the comparison with the radiosonde profile indicated.

In Fig. 7, the optical depth determined from lidar observations at two different zenith angles is compared with star-photometer observations (Leiterer et al. 1995; U. Leiterer 1998, personal communication). Laser pulses were emitted alternately at the two zenith angles of 30° and 60°. At each beam position, signals were taken over 5 min. Signals were then averaged over six successive 5-min measurement periods for each of the two angles. It is believed that in this way small-scale aerosol inhomogeneities are smoothed out. Finally, these mean signal profiles were used to solve Eq. (8). Thus one-hour average values of the optical depths are shown. One has to emphasize that this lidar method works best under horizontal and temporal homogeneous aerosol conditions which is often the case in clear, cloudless nights.

The optical depth shown in Fig. 7 was derived from lidar signals backscattered from the height range between 3500 and 4000 m [see Eq. (9)]. Above 3500-m height, aerosol layers were absent. Optical-depth values could not be calculated for 710 and 1064 nm. At 1064 nm, backscatter signals from the considered regions were too small for detection. The 710-nm channels were used for the depolarization observations. For this reason, they could not be used for the optical-depth determination because the optical detector characteristics change with changing tilt angle. Equation (8) assumes a constant optical efficiency of the system for both measurement angles.

The agreement with the star-photometer observation is quite reasonable. A good consistency is given for the optical-depth values at 355 and 532 nm and for the integrated particle extinction profiles in Fig. 5, if one assumes almost constant particle extinction coefficients for heights below 900 m as indicated by the backscatter profile in Fig. 6. It should be emphasized that overlap problems do not play a role in the optical-depth determination. As a consequence, the values of the optical depth can directly be compared with sun- or star-photometer observations. However, the advantage of the scanning-lidar method is that, in principle, the optical depth of different observed aerosol layers can be resolved and that the method works even in the presence of clouds above the investigated height region. This is not possible with photometers, which always see the entire optical effect between the instrument and the radiation source.

A second example representing an observational period of 2 h is shown in Fig. 8. The data evaluation was identical to the one described above (Fig. 5). A strongly absorbing aerosol layer in the free troposphere could be monitored by aircraft and lidar for more than 36 h. Forest fires in western Canada are believed to be the source of the aerosol. Satellite imagery indicated a large area in the Rocky Mountains covered with smoke at the end of July 1998. From 10-day backtrajectory analysis performed by the German Weather Service it was found that the air masses traveled across North America and Greenland to Europe. It may be interesting to note that the weather services interpreted this aerosol layer as cirrostratus and cirrus uncinus in their routine weather observations. However, according to radiosonde and li-

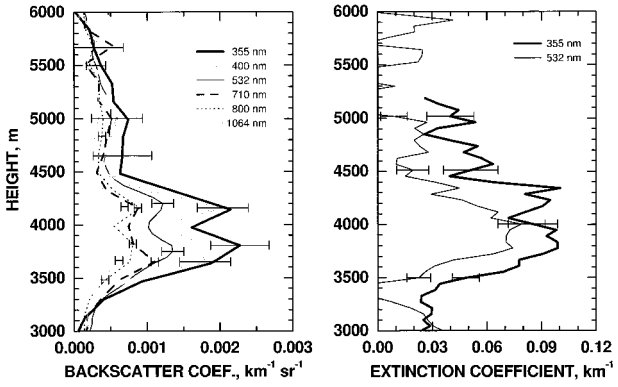

FIG. 8. Mean particle backscatter and extinction coefficients of an aerosol layer in the free troposphere observed on 9 Aug 1998 between 2000 and 2200 UTC. The layer probably originated from forest fires in western Canada and was present over the field site for more than 36 h. The lidar was operated at a zenith angle of 20°. Signal smoothing lengths are 180 (backscatter) and 600 m (extinction). Error bars indicate the standard deviation caused by signal noise and systematic errors.

dar humidity observations the layer was dry with a relative humidity below 40%.

The spectrally resolved backscatter and extinction coefficients as given in Figs. 5 and 7 are used as input parameters for the determination of physical particle parameters such as the volume and surface-area concentrations and the surface-area-weighted mean particle radius. For this retrieval a new inversion scheme has been developed (Müller et al. 1999a,b). Results of inversion calculations are presented in a separate paper. Also given are comparisons with the results obtained from other instruments (Müller et al. 2000).

5. Summary and outlook

A new transportable scanning multiple-wavelength aerosol lidar has been presented. It is optimized for the sounding of tropospheric particles. Laser pulses at 355, 400, 532, 710, 800, and 1064 nm are emitted simultaneously with a repetition rate of 30 Hz. All six laser beams are aligned onto one common optical axis and emitted coaxially with respect to the receiver telescope. This alignment permits one to observe the same atmospheric volume with the same spatial resolution and is a prerequisite for observations under different zenith angles. For these scanning observations a mirror unit that may be set to zenith angles between $+90°$ to $-90°$ is employed. From this technique, profiles may be retrieved close to the ground. From the detection of the elastic-backscatter signals one obtains profiles of 6 backscatter coefficients. The detection of nitrogen Raman signals at 387 and 607 nm and of the water vapor Raman signal at 660 nm provides profiles of extinction coefficients at 355 and 532 nm and of the water vapor mixing ratio, respectively. Detection of the cross- and parallel-polarized signals at 710 nm gives the depolarization-ratio profile. Observation under two different zenith angles permits one to derive optical-thickness profiles and successively even the respective extinction profiles at all six emitted wavelength under favorable atmospheric conditions.

Two measurement examples from LACE 98 showed the capability of the scanning multiwavelength lidar in providing the above-mentioned optical parameters of atmospheric particles. The optical parameter set serves as input for a retrieval scheme that yields physical particle parameters.

The performance characteristics of the system for remote sensing of tropospheric particles are validated in aerosol closure experiments. From simultaneous ground- and aircraft-based in situ and remote-sensing measurement techniques, optical, physical, and chemical particle properties within a well-defined air column are determined. The system has been part of three closure experiments, that is, the Aerosol Characterization Experiment ACE 2 (North Atlantic, Portugal, June–July 1997), the Lindenberg Aerosol Characterization Experiment LACE 98 (Lindenberg, Germany, July–August 1998), and the Indian Ocean Experiment (Maldives, Indian Ocean, February–March 1999). For an entire year the system was used for the investigation of the seasonal variability of tropospheric particles in the Maldives.

REFERENCES

Anderson, S. M., P. Hupalo, and K. Mauersberger, 1993: Ozone absorption cross section measurements in the Wulf bands. *Geophys. Res. Lett.,* **20,** 1579–1582.

Ansmann, A., M. Riebesell, and C. Weitkamp, 1990: Measurements of atmospheric aerosol extinction profiles with a Raman lidar. *Opt. Lett.,* **15,** 746–748.

——, U. Wandinger, M. Riebesell, C. Weitkamp, E. Voss, W. Lahmann, and W. Michaelis, 1992a: Combined Raman elastic-backscatter lidar for vertical profiling of moisture, aerosol extinction, backscatter, and lidar ratio. *Appl. Phys. B,* **55,** 18–28.

——, M. Riebesell, U. Wandinger, C. Weitkamp, and W. Michaelis, 1992b: Independent measurement of extinction and backscatter profiles in cirrus clouds by using a combined Raman elastic-backscatter lidar. *Appl. Opt.,* **29,** 3266–3272.

——, and Coauthors, 1993: Lidar network observations of cirrus morphological and scattering properties during the International Cirrus Experiment 1989: The 18 October 1989 case study and statistical analysis. *J. Appl. Meteor.,* **32,** 1608–1622.

Belan, B. D, A. V. El'nikov, V. V. Zuev, V. E. Zuev, E. V. Makienko, and V. N. Marichev, 1992: Results of investigations of the optical and microstructural characteristics of stratospheric aerosol using the method of lidar measurement inversion over Tomsk in summer 1991. *Atmos. Oceanic Opt.,* **5,** 373–378.

Beyerle, G., R. Neuber, O. Schrems, F. Wittrock, and B. Knudson, 1994: Multiwavelength lidar measurements of stratospheric aerosols above Spitsbergen during winter 1992/93. *Geophys. Res. Lett.,* **21,** 57–60.

Brackmann, U., 1994: *Lambdachrome Laser Dyes.* Lambda Physik GmbH, 272 pp.

Burkholder, J. B., and R. K. Talukdar, 1994: Temperature dependence of the ozone absorption spectrum over the wavelength range 410 to 760 nm. *Geophys. Res. Lett.,* **21,** 581–584.

Burlakov, V. D., A. V. El'nikov, V. V. Zuev, V. N. Marichev, V. L. Pravdin, E. V. Sharabarin, and V. B. Shcheglov, 1992: Multifrequency lidar on the basis of the telescope with the receiving

mirror 2.2 m in diameter for simultaneous sounding of vertical distributions of ozone and aerosol in the stratosphere. *Atmos. Oceanic Opt.,* **5,** 664–667.

Chaikovsky, A. P., I. S. Hutko, A. P. Ivanov, F. P. Osipenko, V. N. Shcherbakov, and S. B. Tauroginskaya, 1994: Multi-wavelength laser sounding of the troposphere over continental regions. *Proc. 17th Int. Laser Radar Conf.,* Sendai, Japan, 87–88.

Charlson, R. J., and J. Heintzenberg, Eds., 1995: *Aerosol Forcing of Climate.* John Wiley, 416 pp.

——, S. E. Schwartz, J. M. Hales, R. D. Cess, J. A. Coakley Jr., J. E. Hansen, and D. J. Hofmann, 1992: Climate forcing by anthropogenic aerosols. *Science,* **255,** 423–430.

Clauder, E., 1996: Konzeption und Aufbau einer Strahlseparationseinheit für ein Mehrwellenlängenlidar. Diploma thesis, Universität Leipzig, 62 pp. [Available from Institute for Tropospheric Research, Permoserstr. 15, 04318 Leipzig, Germany.]

DelGuasta, M., M. Morandi, L. Stefanutti, and J. P. Wolf, 1994a: Derivation of Mount Pinatubo stratospheric aerosol mean size distribution by means of a multiwavelength lidar. *Appl. Opt.,* **33,** 5690–5725.

——, and Coauthors, 1994b: Multiwavelength lidar observation of thin cirrus at the basis of the Pinatubo stratospheric layer during the EASOE campaign. *Geophys. Res. Lett.,* **21,** 1339–1342.

Deshler, T., B. J. Johnson, and W. R. Rozier, 1993: Balloonborne measurements of Pinatubo aerosol during 1991 and 1992 at 41°N: Vertical profiles, size distribution, and volatility. *Geophys. Res. Lett.,* **20,** 1435–1438.

Eloranta, E. W., and P. Piironen, 1997: Measurements of cirrus cloud optical properties and particle size with the University of Wisconsin High Spectral Resolution Lidar. *Advances in Atmospheric Remote Sensing with Lidar,* A. Ansmann et al., Eds., Springer, 83–86.

Evans, B. T. N., 1987: Sensitivity of the backscatter/extinction ratio to changes in aerosol properties: implications for lidar. *Appl. Opt.,* **27,** 3299–3305.

Exciton, 1989: *Laser Dye Catalog.* Exciton Inc., 40 pp.

Fernald, F. G., 1984: Analysis of atmospheric lidar observations: some comments. *Appl. Opt.,* **23,** 652–653.

Ferrare, R. A., S. H. Melfi, D. N. Whiteman, K. D. Evans, and R. Leifer, 1998a: Raman lidar measurements of aerosol extinction and backscattering, 1. Methods and comparisons. *J. Geophys. Res.,* **103,** 19 663–19 672.

——, ——, ——, ——, and ——, 1998b: Raman lidar measurements of aerosol extinction and backscattering, 2. Derivation of aerosol real refractive index, single-scattering albedo, and humidification factor using Raman lidar and aircraft size distribution measurements. *J. Geophys. Res.,* **103,** 19 673–19 689.

Grund, C. J., and E. W. Eloranta, 1991: The University of Wisconsin High Spectral Resolution Lidar. *Opt. Eng.,* **30,** 6–12.

Gutkowicz-Krusin, D., 1993: Multiangle lidar performance in the presence of horizontal inhomogeneities in atmospheric extinction and scattering. *Appl. Opt.,* **32,** 3266–3272.

Hamilton, P. M., 1969: Lidar measurement of backscatter and attenuation of atmospheric aerosol. *Atmos. Environ.,* **3,** 221–223.

Heintzenberg, J., H. Müller, H. Quenzel, and E. Thomalla, 1981: Information content of optical data with respect to aerosol properties: numerical studies with a randomized minimization-search-technique inversion algorithm. *Appl. Opt.,* **20,** 1308–1315.

——, H.-F. Graf, R. J. Charlson, and P. Warneck, 1996: Climate forcing and the physico-chemical life cycle of the atmospheric aerosol—Why do we need an integrated interdisciplinary global research program? *Contrib. Atmos. Phys.,* **69,** 261–271.

Hobbs, P. V., and B. J. Huebert, Eds., 1996: Atmospheric aerosols. A new focus of the International Global Atmospheric Chemistry Project (IGAC). IGAC Core Project Office, Massachusetts Institute of Technology, 40 pp. [Available from IGAC Core Project Office, Building 24-409, Massachusetts Institute of Technology, Cambridge, MA 02139-4307.]

Ivanov, A. P., F. P. Osipenko, A. P. Chaikovskiy, and V. N. Shcherbakov, 1986: Study of the aerosol optical properties and microstructure by the method of multiwave sounding. *Izv. Atmos. Oceanic Phys.,* **22,** 633–639.

Karl, T. R., and Coauthors, 1993: A new perspective on recent global warming. *Bull. Amer. Meteor. Soc.,* **74,** 1007–1023.

Kiel, J. T., and B. P. Briegleb, 1993: The relative roles of sulfate aerosols and greenhouse gases. *Science,* **260,** 311–314.

Klett, J. D., 1981: Stable analytical inversion solution for processing lidar returns. *Appl. Opt.,* **20,** 211–220.

——, 1985: Lidar inversion with variable backscatter/extinction ratios. *Appl. Opt.,* **24,** 1638–1643.

Kolenda, J., and Coauthors, 1992: Aerosol size distribution measurements using a multispectral lidar system. *Lidar for Remote Sensing,* R. J. Becherer, R. M. Hardesty, and J. P. Meyzonette, Eds., *Proc. SPIE,* **1714,** 209–219.

Leiterer, U., A. Naebert, T. Naebert, and G. Alekseeva, 1995: A new star photometer developed for spectral aerosol optical thickness measurements in Lindenberg. *Contrib. Atmos. Phys.,* **68,** 133–141.

Makiyenko, E. V., and I. E. Naats, 1983: Determination of the optical properties of the stratospheric aerosols by multifrequency laser sensing. *Izv. Atmos. Oceanic Phys.,* **19,** 748–751.

McCormick, P., 1982: Lidar measurements of Mount St. Helens effluents. *Opt. Eng.,* **21,** 340–342.

McKenzie, R. L., and Coauthors, 1994: Multi-wavelength profiles of aerosol backscatter over Lauder, New Zealand, 24 November 1992. *Geophys. Res. Lett.,* **21,** 789–792.

Melfi, S. H., J. D. Lawrence, and M. P. McCormick, 1969: Observation of Raman scattering by water vapor in the atmosphere. *Appl. Phys. Lett.,* **15,** 295–297.

Molina, L. T., and M. J. Molina, 1986: Absolute absorption cross sections of ozone in the 185- to 350-nm wavelength range. *J. Geophys. Res.,* **91,** 14 501–14 508.

Müller, D., U. Wandinger, D. Althausen, I. Mattis, and A. Ansmann, 1998: Retrieval of physical particle properties from lidar observations of extinction and backscatter at multiple wavelengths. *Appl. Opt.,* **37,** 2260–2263.

——, ——, and A. Ansmann, 1999a: Microphysical particle parameters from extinction and backscatter lidar data by inversion with regularization: Theory. *Appl. Opt.,* **38,** 2346–2357.

——, ——, and ——, 1999b: Microphysical particle parameters from extinction and backscatter lidar data by inversion with regularization: Simulation. *Appl. Opt.,* **38,** 2358–2368.

——, F. Wagner, D. Althausen, U. Wandinger, M. Wendisch, A. Keil, and A. Ansmann, 2000: Microphysical particle parameters from extinction and backscatter lidar data by inversion with regularization: Experiment. *Appl. Opt.,* **39,** 1879–1892.

Müller, H., 1981: Die Bestimmbarkeit der atmosphärischen Aerosolgrößenverteilung mit Hilfe eines 4-Wellenlängen-Lidars. Ph.D. dissertation, Wissenschaftliche Mitteilung Nr. 44, Universität München, 99 pp. [Available from Münchener Universitäts-Schriften, Fachbereich Physik, Theresienstr. 37, 80333 München, Germany.]

Naats, I. E., 1980: *The Theory of Multifrequency Sounding of the Atmosphere* (in Russian). Nauka, 157 pp.

Ontar Corporation, 1994: HITRAN Optical Spectroscopy Database. ONTAR Corporation, 190 pp. [Available from Ontar Corp., 9 Village Way, North Andover, MA 01845.]

Penner, J. E., R. E. Dickinson, and C. A. O'Neill, 1992: Effects of aerosols from biomass burning on the global radiation budget. *Science,* **256,** 1432–1434.

Piironen, P., and E. W. Eloranta, 1994: Demonstration of a high spectral resolution lidar based on an iodine absorption filter. *Opt. Lett.,* **19,** 234–236.

Post, M. J., C. J. Grund, A. M. Weickmann, K. R. Healy, and R. J. Willis, 1996: Comparison of Mount Pinatubo and El Chichon volcanic events: Lidar observations at 10.6 and 0.69 μm. *J. Geophys. Res.,* **101,** 3929–3940.

——, ——, D. Wang, and T. Deshler, 1997: Evolution of Mount Pinatubo's aerosol size distributions over the continental United

States: Two wavelength lidar retrievals and in situ measurements. *J. Geophys. Res.*, **102,** 13 535–13 542.

Qing, P., H. Nakane, Y. Sasano, and S. Kitamura, 1989: Numerical simulation of the retrieval of aerosol size distribution from multiwavelength laser radar measurements. *Appl. Opt.*, **28,** 5259–5265.

Quinn, P. K., and Coauthors, 1996: Closure in tropospheric aerosol-climate research: A review and future needs for addressing aerosol direct shortwave radiative forcing. *Contrib. Atmos. Phys.*, **69,** 547–577.

Reiter, R., M. Litfaß, M. Carnuth, and W. Funk, 1979: Lidar measurements of concentration and size distribution profiles of tropospheric aerosol. *Proc. 9th Int. Laser Radar Conf.*, Munich, Germany, 82–84.

Sasano, Y., and E. V. Browell, 1989: Light scattering characteristics of various aerosol types derived from multiple wavelength lidar observations. *Appl. Opt.*, **28,** 1670–1679.

——, ——, and S. Ismail, 1985: Error caused by using a constant extinction/backscatter ratio in the lidar solution. *Appl. Opt.*, **24,** 3929–3932.

Sassen, K., 1991: The polarization lidar technique for cloud research: A review and current assessment. *Bull. Amer. Meteor. Soc.*, **72,** 1848–1866.

Schneider, W., G. K. Moortgart, G. S. Tyndall, and J. P. Burrows, 1987: Absorption cross-sections of NO_2 in the UV and visible region (200–700 nm) at 298 K. *J. Photochem. Photobiol., A,* **40,** 195–217.

Schotland, R. M., K. Sassen, and R. Stone, 1971: Observations by lidar of linear depolarization ratios for hydrometeors. *J. Appl. Meteor.*, **10,** 1011–1017.

Shipley, S. T., D. H. Tracy, E. W. Eloranta, J. T. Trauger, J. T. Sroga, F. L. Roesler, and J. A. Weinman, 1983: High spectral resolution lidar to measure optical scattering properties of atmospheric aerosols. 1: Theory and instrumentation. *Appl. Opt.*, **22,** 3717–3724.

Sidebottom, H. W., C. C. Badcock, G. E. Jackson, J. G. Calvert, G. W. Reinhardt, and E. K. Damon, 1972: Photooxidation of sulfur dioxide. *Environ. Sci. Technol.*, **6,** 72–79.

Spinhirne, J. D., S. Chudamani, J. F. Cavanaugh, and J. L. Bufton, 1997: Aerosol and cloud backscatter at 1.06, 1.54, and 0.53 μm by airborne hard-target-calibrated Nd:YAG/methane Raman lidar. *Appl. Opt.*, **36,** 3475–3490.

Sroga, J. T., E. W. Eloranta, S. T. Shipley, F. L. Roesler, and P. J. Tryon, 1983: High spectral resolution lidar to measure optical scattering properties of atmospheric aerosols. 2: Calibration and data analysis. *Appl. Opt.*, **22,** 3725–3732.

Stefanutti, L., and Coauthors, 1992: A four-wavelength depolarization backscattering lidar for polar stratospheric cloud monitoring. *Appl. Phys. B,* **55,** 13–17.

Stein, B., M. DelGuasta, J. Kolenda, M. Morandi, P. Rairoux, L. Stefanutti, J. P. Wolf, and L. Wöste, 1994: Stratospheric aerosol size measurements at Sodankylä during EASOE. *Geophys. Res. Lett.*, **21,** 1311–1314.

Uthe, E. E., B. M. Morley, and N. B. Nielsen, 1982: Airborne lidar measurements of smoke plume distribution, vertical transmission, and particle size. *Appl. Opt.*, **21,** 460–462.

Veretennikov, V. V., V. S. Kozlov, I. E. Naats, and V. Ya. Fadeev, 1979: Optical studies of smoke aerosols: an inversion method and its applications. *Opt. Lett.*, **4,** 411–413.

Wallenhauer, S., 1998: Bestimmung spektraler Streukoeffizienten des atmosphärischen Aerosols aus Lidarmessungen. Diploma thesis, Universität Leipzig, 52 pp. [Available from Institute for Tropospheric Research, Permoserstr. 15, 04318 Leipzig, Germany.]

Zuev, V. E., and I. E. Naats, 1983: *Inverse Problems of Lidar Sensing of the Atmosphere.* Springer, 260 pp.